ACS APPLIED MATERIALS & INTERFACES

www.acsami.org

Research Article

# Bio-Inspired Preparation of Clay−Hexacyanoferrate Composite Hydrogels as Super Adsorbents for $Cs^+$

Huagui Zhang,* Chris S. Hodges, Prashant Kumar Mishra, Ji Young Yoon, Timothy N. Hunter, Jae W. Lee, and David Harbottle*

**Cite This:** *ACS Appl. Mater. Interfaces* 2020, 12, 33173−33185

**Read Online**

ACCESS | Metrics & More | Article Recommendations | Supporting Information

**ABSTRACT:** A facile and low-cost fabrication route, inspired by the adhesive proteins secreted by mussels, has been developed to prepare a clay-based composite hydrogel (DHG(Cu)) containing hexacyanoferrate (HCF) nanoparticles for the selective removal of $Cs^+$ from contaminated water. Initially, montmorillonite was exfoliated prior to coating with a thin layer of polydopamine (PDOPA) via the self-polymerization of dopamine. Mixing the composite (D-clay) with the HCF precursor, followed by the addition of copper ions, led to the self-assembly of the polymer-coated exfoliated clay nanosheets into a three-dimensional network and in situ growth of KCuHCF nanoparticles embedded within the gel structure. Analytical characterization verified the fabrication route and KCuHCF immobilization by a copper−ligand complexation. Rheology testing revealed the composite hydrogel to be elastic under low strain and exhibited reversible, self-healing behavior following high strain deformation, providing a good retention of KCuHCF nanoparticles in the membrane. The adsorbent DHG(Cu) showed a superior $Cs^+$ adsorption capacity (∼173 mg/g), with the performance maintained over a wide pH range, and an excellent selectivity for $Cs^+$ when dispersed in seawater at low concentrations of 0.2 ppm. On the basis of its excellent mechanico-chemical properties, the fabricated hydrogel was tested as a membrane in column filtration, showing excellent removal of $Cs^+$ from Milli-Q water and seawater, with the performance only limited by the fluid residence time. For comparison, the study also considered other composite hydrogels, which were fabricated as intermediates of DHG(Cu) or fabricated with $Fe^{3+}$ as the cross-linker and reactant for HCF nanoparticle synthesis.

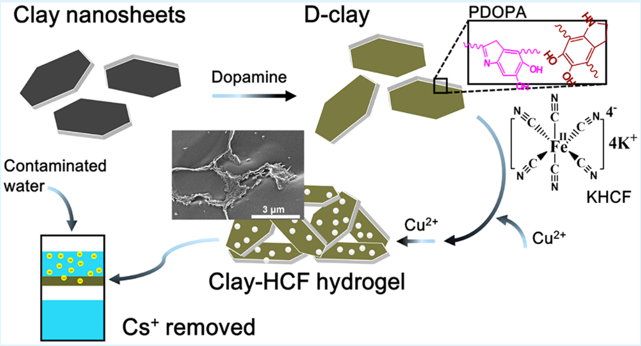

**KEYWORDS:** *cesium adsorbent, hexacyanoferrate, clay nanosheets, decontamination, hydrogel membrane*

## 1. INTRODUCTION

Nuclear power remains an effective energy source of relatively low cost and minimal waste generation during routine operation. However, the accumulation of legacy wastes and the potential for extensive contamination of ground and groundwater systems following an incident, such as Chernobyl and Fukushima, are cause for concern, and new materials are desired to aide in the cleanup following such incidents.[1−7]

The removal of $^{137}Cs$ is particularly studied due to its high abundance, relatively long half-life (30 years), and high solubility in aqueous media. Removal strategies can include chemical precipitation, membrane extraction, and ion exchange, with the removal performance assessed based on capacity, selectivity, and kinetics. Ion sorption by selective sorbents has been widely considered with a range of materials tested and used to recover $Cs^+$ from aqueous systems such as vanadosilicate,[8] chalcogenides,[9] zeolite,[10,11] clay,[12] and layered double hydroxides (LDHs).[13]

Analogues of Prussian blue (PBA), for example potassium copper hexacyanoferrate (KCuHCF),[14] have been shown to give excellent sorption capacity and selectivity for $Cs^+$ due to its cubic network of iron centers bound by a bridging cyanide ligand, acting as an ion-sieve for small hydrated ions of a specific size (3.2 Å), where $Cs^+$ is able to permeate the lattice structure while larger competing ions are blocked.[2,3,15] The practical use of this excellent material has been limited due to its extremely small particle size, ∼10 nm; as such, various material supports have been fabricated to immobilize HCF nanoparticles, including the polymer matrix of chitin beads,[15] alginate,[16] and poly(acrylic acid);[17] nanoclusters[18] and porous media of mesoporous silica;[3] graphene oxide foam;[19] and hydrogels.[2,20] Among the various material supports, hydrogels and composite hydrogels have shown great promise in water

**Received:** April 10, 2020
**Accepted:** June 12, 2020
**Published:** June 12, 2020

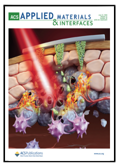

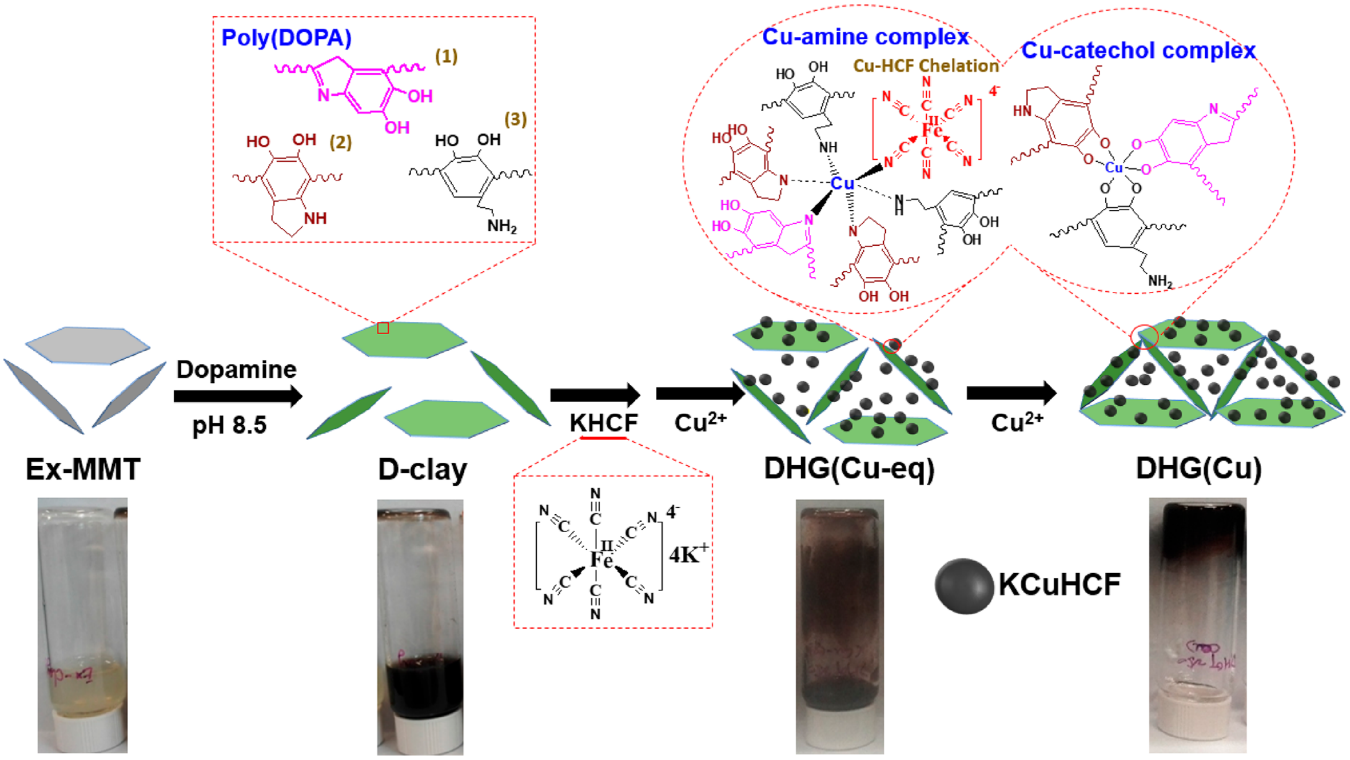

**Figure 1.** (Top) D-clay/HCF composite hydrogel preparation with illustrations of the possible existing forms of poly(dopamine) and their coordination mechanisms with Cu. (Bottom) From left to right, images of the pristine exfoliated clay (Ex-MMT), D-clay, intermediate product DHG(Cu-eq), and HCF/D-clay composite hydrogel DHG(Cu).

treatment applications for removing heavy metal ions and organic contaminants,[16,21−25] with the performance attributed to their open-porous structure of 3D-hydrophilic networks that facilitate a high water flux. However, most hydrogels are fabricated using polymers that are covalently cross-linked,[16,21−23,25] with these materials susceptible to radiation damage.[21,22] Therefore, there is a need for modified hydrogels, such as composite hydrogels that incorporate significant inorganic content, to exhibit mechanical stability in radioactive applications.

Dopamine (DOPA), a natural catecholamine, can be polymerized into polydopamine (PDOPA) to form adhesive coatings on various substrates.[23] PDOPA possess various functional groups such as *o*-quinone, carboxy, amino, imine, and phenol groups that are amenable to metal-ion binding. For instance, catechol-ferric ion coordination has recently been exploited to develop organic hydrogels based on catechol-modified polymers,[24,25] and inorganic hydrogels based on PDOPA coated nanostructures with $Fe^{3+}$ as cross-linker.[26,27]

The current study reports the fabrication and performance testing of an inorganic−organic composite hydrogel with HCF nanoparticles immobilized to recover $Cs^+$ from contaminated water. Montmorillonite (MMT) clay nanosheets were used to form a 3D structure and serve as a support to anchor the HCF nanoparticles. The in situ synthesis of KCuHCF was carried out wherein $Cu^{2+}$ acts as both a reactant for HCF nanoparticles and a cross-linker for PDOPA coated on clays to assemble the coated clay nanosheets into a 3D gel framework. The coordination between $Cu^{2+}$ and PDOPA-coated clay increases the hydrogel strength[23] and provides binding sites for KCuHCF nanoparticles. The fabricated composite hydrogels demonstrated both excellent absorption of $Cs^+$ and enhanced mechanical properties for application as a filtration membrane.

The composite hydrogel was characterized by Fourier transform infrared spectroscopy (FTIR), powder X-ray diffraction (XRD), and cryo-scanning electron microscopy (Cryo-SEM), and performance was tested in batch and flow-through systems in the absence and presence of competitive ions.

## 2. EXPERIMENTAL SECTION

**2.1. Chemicals.** Montmorillonite clay (MMT) of a ∼200 mesh size (<74 $\mu$m) was purchased from Alfa Aesar. Dopamine hydrochloride (DOPA·HCl), tris(hydroxymethyl)aminomethane (>99.8%, $C_4H_{11}NO_3$, TRIS), potassium hexacyanoferrate ($K_4[Fe(CN)_6]\cdot 3H_2O$), copper sulfate ($CuSO_4\cdot 5H_2O$), and cesium chloride (CsCl, analytical grade) were purchased from Sigma-Aldrich and used as-received.

The cation exchange capacity (CEC) of montmorillonite was 90 mequiv/100 g based on the sorption of the 0.01 M Cu(II)−triethylenetetramine complex $[Cu\ Trien]^{2+}$ following the procedure outlined by Honty et al.,[28] with the concentration measured at 577 nm using UV spectroscopy (UV-1800 SHIMADZU). The Brunauer−Emmett−Teller (BET) specific surface area of montmorillonite particles was 29.85 $m^2/g$, as determined by a $N_2$ adsorption isotherm (Micromeritics TriStar 3000). The chemical composition of montmorillonite was determined by X-ray fluorescence (XRF) spectrometry and was found to be 2.20 $Na_2O$, 2.39 MgO, 20.80 $Al_2O_3$, 66.86 $SiO_2$, 0.06 $P_2O_5$, 0.40 $SO_3$, 0.70 $K_2O$, 1.66 CaO, 0.16 $TiO_2$, 0.05 MnO, 4.57 $Fe_2O_3$, 0.03 CuO, 0.01 ZnO, 0.06 SrO, and 0.05 wt % $ZrO_2$.

**2.2. Synthesis.** *2.2.1. Exfoliation of MMT.* Under gentle agitation, montmorillonite particles were dispersed in ultrapure Milli-Q water (resistivity of 18.2 MΩ cm) at a solid-to-liquid ratio of 30 g/L and left undisturbed for 12 h to separate the quartz sand and heavy minerals. The remaining stable suspension (nonsedimented MMT) was decanted and ultrasonicated for 1 h at 40% amplitude using a Sonic Dismembrator (Model FB-505 Fisher Scientific) in four 15 min intervals to avoid significant sample heating. Due to anisotropic bonding (i.e., strong in-plane and weak out-of-plane bonding), MMT swells in water by increasing the interlayer spacing. By ultrasonication, the silicate plates can be exfoliated into individual platelets of a nm thickness.[29,30] The exfoliated MMT particles were centrifuged at 2000 rpm for 10 min to remove any unexfoliated particles. The resultant suspension was collected, and the particle concentration was determined by dry mass measurement, with the sample named Ex-MMT and stored for subsequent use.

*2.2.2. Preparation of D-Clay.* TRIS (121.1 mg) was dissolved in 100 mL of an Ex-MMT suspension at pH 8.5, and 130.4 mg of DOPA (161.5 mg of DOPA HCl) was subsequently added to the suspension mixture, followed by stirring for 2 h. When adding DOPA to Ex-MMT, the suspension gradually changed from brown to black. As reported in earlier studies,[31,32] to remove any unbound polydopamine from PDOPA-coated nanoparticles, the suspension was centrifuged at 13000 rpm for 50 min and washed with Milli-Q water at least 3 times until the supernatant appeared transparent. The solid content of the resulting D-clay suspension was 10.6 g/L. Pure PDOPA was prepared as a test standard by self-polymerization under identical conditions (TRIS buffer addition at pH 8.5) in the absence of Ex-MMT.

*2.2.3. Composite Hydrogel Fabrication.* A D-clay/HCF composite hydrogel was prepared via a three-step process from Ex-MMT, as shown in Figure 1. After preparing D-clay, 2 mL of 0.25 M $K_4Fe(CN)_6$ (abbreviated as KHCF) was added to 16 mL of a D-clay suspension (solids content = 7.55 g/L) in a glass beaker and magnetically stirred for 2 h at ambient conditions. Then, 2 mL of 0.25 M $CuSO_4$ was added dropwise (stoichiometric equivalence of Cu and KHCF) under stirring and allowed to react for 2 h. The resulting product was named DHG(Cu-eq), which remained as a viscous, reddish-brown suspension containing KCuHCF nanoparticles, see Figure 1. In the second step, 0.4 mL of $CuSO_4$ (1 M) was added to the viscous suspension to promote the assembly of MMT nanosheets (via cross-linking between PDOPA-coated MMT nanosheets by $Cu^{2+}$) into a 3D structure, with black hydrogels formed within minutes, denoted as DHG(Cu), see Figure 1. The water content of the as-prepared hydrogel was measured by dry mass and found to be 97.3 wt %.

Moreover, to study how the cross-linker ($Cu^{2+}$or $Fe^{3+}$) and fabrication method (addition sequence of reactants, either KHCF or $Cu^{2+}$ first to D-clay) affected the mechanical property and adsorption performance of the composite hydrogel, additional samples were prepared for comparison. DHG(Fe) was prepared with $FeCl_3$ replacing $CuSO_4$ throughout the composite hydrogel preparation. DHG(step Cu) and DHG(step Fe) were both prepared by adding $CuSO_4$ prior to KHCF in the first step and cross-linking by $CuSO_4$ and $FeCl_3$ in the second step, respectively. In addition, the pure D-clay hydrogel without KCuHCF nanoparticles was prepared as a control sample, named DG(Cu). More details on the fabrication methods are given in Supporting Information.

**2.3. Materials Characterization.** *2.3.1. Atomic Force Microscope (AFM).* Images of exfoliated MMT nanosheets and pristine clay particles were acquired in tapping mode using an Innova AFM (Bruker, USA), scanning at 0.3 Hz with a TAP300 40 N/m silicon cantilever (Bruker, USA). Samples were prepared by depositing one drop of 10 ppm Ex-MMT or pristine clay suspension (at neutral pH) on a freshly cleaved mica surface and dried at room temperature before imaging. Height profile measurements were made by imaging several nanosheets and clay particles.

*2.3.2. Cryo-SEM.* Hydrated hydrogels were imaged using Cryo-SEM (PP3010T, Quorum Technologies, UK). Approximately 0.5 g of hydrogel was deposited on a 0.1 cm diameter universal specimen shuttle (AL200077B) and plunged into liquid nitrogen at $T = -196$ °C. The sample was transferred to the Quilo cryo-preparation chamber ($T = -175$ °C) using the cryo-transfer device under vacuum. The cryo-preparation chamber had several viewing windows to carefully remove excess ice using the twin fracturing tool manipulators before transferring the sample from the cryo-preparation chamber to the highly stable SEM cold stage for observation. Cold trapping in the cryo-preparation and SEM chambers ensured the sample handling and preparation were frost-free. Elemental mapping of samples was completed using an Oxford Instruments INCA 350 energy dispersive X-ray spectrometer (EDX) with an 80 mm X-Max SDD detector, equipped within the FEGSEM instrument.

*2.3.3. Powder X-ray Diffraction (PXRD).* PXRD patterns were collected using a Bruker D8 X-ray diffractometer fitted with a LynxEye detector and a Cu K$\alpha$ (1.54 Å) radiation source operating at 40 kV and 40 mA, which was calibrated to a Si standard. Each sample was scanned between $2\theta$ angles from 4 to 70° with a step size of 0.03299° at 2 s/step. Hydrogels were dried under a slight vacuum (pressure <10 kPa) at 60 °C for 24 h and crushed to powder for characterization. For Ex-MMT, to avoid restacking during drying, the sample remained wet, and the XRD pattern was measured using a Philips X'Pert X-ray diffractometer. For comparison, pristine MMT was also characterized as a wet sample.

*2.3.4. Fourier Transform Infrared (FT-IR).* A Nicolet iS10 FT-IR spectrometer equipped with a deuterated triglycine sulfate (DTGS) KBr detector was used to measure the FTIR spectra of D-clay and the dried composite hydrogel DHG(Cu) with pure PDOPA and pristine clay as the reference. A minimum of 36 scans was performed at the average infrared signal with a resolution of 4 $cm^{-1}$ in the range 600 $cm^{-1}$ to 4000 $cm^{-1}$.

*2.3.5. Thermogravimetric Analysis (TGA).* Samples of ca. 20 mg were measured using a Mettler-Toledo TGA-DSC1 instrument. A standard heating profile from 30 to 900 °C at a heating rate of 10 °C/min under steady $N_2$ flow (50 mL/min) was used for all samples. The collected data were blank subtracted.

*2.3.6. X-ray Photoelectron Spectroscopy (XPS).* The sample chemical bonds were analyzed using a Thermo K-Alpha XPS system with a monochromated Al K$\alpha$ X-ray source. An electron/ion gun was used to compensate for charge build-up on the sample during measurement. The XPS peaks were fitted using the CasaXPS software, and the binding energy was corrected with a reference to C 1s at 284.5 eV.

*2.3.7. Inductively Coupled Plasma-Optical Emission Spectroscopy (ICP-OES).* The metal content of the composite hydrogel was measured by ICP-OES (ICP-OES 720, Agilent, USA). The composite hydrogel was mineralized using a mixture of nitric and hydrochloric acid at elevated temperatures, and the sample solution was scanned over multiple wavelengths, with elements detected at specific emission wavelengths (Cu, 327.395; Fe, 238.204; K, 769.897; and Na, 589.592 nm). The quantification for each peak was done via peak-area analysis with background correction for the blank.

*2.3.8. Rheology.* The rheology of the fabricated hydrogels was measured using a DHR-2 controlled-stress rheometer (TA Instruments, USA), with a 25 mm diameter parallel plate. The geometry gap was set to 1 mm. Strain sweep tests were performed at 1 rad/s, and frequency sweep tests were performed in the linear viscoelastic regime with a strain amplitude of 1%. To measure the relaxation/recovery of hydrogels in response to an applied shear strain, the following protocol was used (applied shear strain with the duration in parentheses): 0.1 (300), 1000 (300), 0.1 (600), 1000 (300), 0.1 (600), 1000 (300), and 0.1% (1200 s). All measurements were conducted at $T = 23$ °C.

**2.4. HCF Nanoparticle Stability.** To assess the stability of HCF nanoparticles (e.g., KCuHCF or PB(KFeHCF) nanoparticles) within the fabricated hydrogels, the hydrogels were broken under vigorous vortex-stirring, and the solids were separated from the liquid by centrifuging at 9500 rpm for 15 min. The decanted supernatant was analyzed using UV−vis spectroscopy (UV-1800 SHIMADZU), and the concentration of KCuHCF or PB(KFeHCF) nanoparticles was determined by calibration curves at 479 and 689 nm, corresponding to the adsorption bands of KCuHCF and PB(KFeHCF), respectively (see Figure S2). The dispersing and washing protocols were repeated 8 times.

**2.5. $Cs^+$ Adsorption.** *2.5.1. Batch Adsorption.* Tests were conducted using plastic vials to avoid Si contamination from the glassware and any potential $Cs^+$ adsorption onto the glassware, as previously reported.[33] The solid content was 1 g/L in 20 mL of liquid, based on a solid fraction of 2.7 wt % of the fabricated hydrogel (water

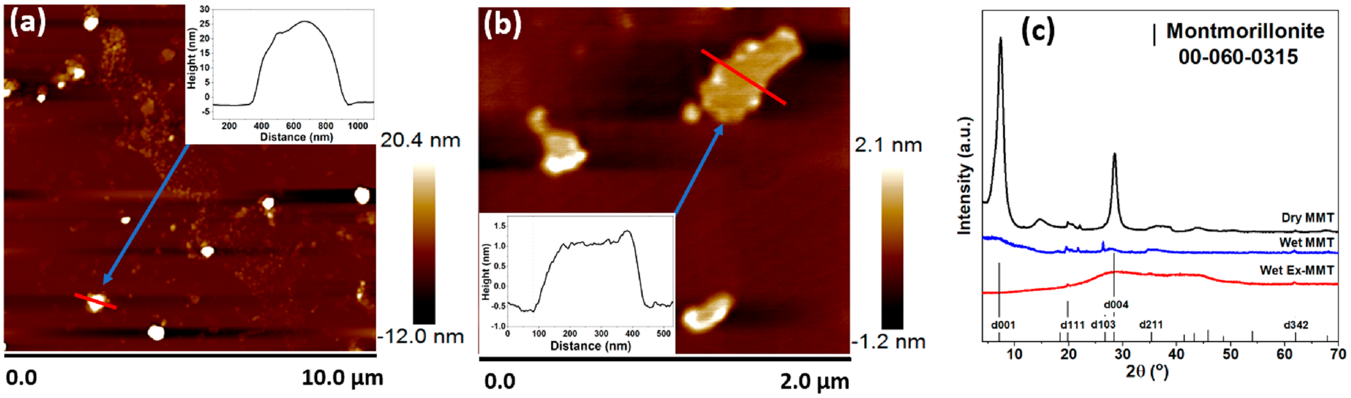

**Figure 2.** Tapping-mode AFM images of (a) pristine MMT and (b) Ex-MMT nanosheets deposited on fresh mica. (c) XRD patterns of pristine MMT and Ex-MMT in Milli-Q water (Wet).

content 97.3 wt %). Cesium chloride (CsCl) solutions with $Cs^+$ concentrations varying from 5 to 400 ppm were prepared individually in polypropylene centrifuge tubes by diluting a 1000 ppm CsCl stock solution. The fabricated hydrogels (in wetted) were added to the $Cs^+$ solutions and mixed using an orbital shaker at 200 rpm for 24 h. Sample tubes were centrifuged for 15 min at 11000 rpm, and the supernatant was decanted and passed through a 0.45 $\mu$m syringe filter. The concentration of $Cs^+$ in the supernatant was measured by inductively coupled plasma mass spectroscopy (ICP-MS, PerkinElmer Elan DRCe). The concentration was first calibrated using a CsCl standard solution of known concentrations from 0.5 to 20 ppm.

The amount of $Cs^+$ adsorbed by the solids, $q$ (mg/g), was determined using the following equation:

$$q = \frac{(C_0 - C_e)V}{m} \tag{1}$$

where $C_0$ and $C_e$ (ppm) are the initial and equilibrium $Cs^+$ concentrations, respectively (determined by ICP-MS); $V$ (mL) is the volume of the suspension; and $m$ (g) is the amount of the adsorbent (mass of the solid fraction of the hydrogel).

Adsorption kinetics were measured using a fixed initial $Cs^+$ concentration ($C_0$) of 100 ppm, with the adsorption time varying from 10 min to 24 h. All adsorption tests were conducted under neutral conditions, except for the pH-dependent study. For the pH-dependent study, the DHG(Cu) composite hydrogel was tested across a pH range of 2 to 12 with $C_0$ = 300 ppm. The pH was adjusted using 1.0 M HCl or 1.0 M NaOH. All other experimental parameters remained consistent with those previously described (solid-to-liquid ratio of 1 g/L, with shaking at 200 rpm for 24 h).

The $Cs^+$ selectivity in the presence of competitive ions was studied by dispersing composite hydrogels (1 g/L) in 20 mL of seawater (untreated composition: $Na^+$, ∼12500; $Mg^{2+}$, ∼1480; $K^+$, ∼480; $Ca^{2+}$, ∼150 ppm)[34] containing 0.2 ppm $Cs^+$. The samples were shaken for 24 h prior to separation and analysis of the supernatant to determine the $Cs^+$ concentration measured by ICP-MS.

*2.5.2. Filtration.* Using a 20 mL plastic syringe, the DHG(Cu) hydrogel was gently placed onto a prewetted (Milli-Q water) polyether sulfone (PES) membrane filter (pore size 0.22 $\mu$m, water flux above 500 L/($m^2$ h), supplied by Millipore) to form a uniformly thick membrane. The hydrogel was then left quiescent for 1 h prior to testing to ensure there were no defects/voids in the hydrogel membrane. Then, 20 mL of a 0.5 ppm $Cs^+$ solution was slowly poured into the syringe with the filtered liquid collected and analyzed by ICP-MS to determine the resulting $Cs^+$ concentration. The mass of the DHG(Cu) hydrogel added to the syringe was varied from 0.5 to 6.0 g, with the liquid volume fixed at 20 mL. Liquid filtration occurred without any external pressure.

## 3. RESULTS AND DISCUSSION

**3.1. Preparation and Characterization of D-Clay/HCF Hydrogels.** Pristine MMT was exfoliated into nanosheets by ultrasonication. Figure 2 shows the morphology (measured by AFM imaging) of pristine MMT (Figure 2a) and Ex-MMT nanosheets (Figure 2b). Height profiles of the nanosheets revealed the thickness to be ∼1 nm, confirming single-layers for Ex-MMT. For pristine MMT, height profiles were quite varied, with peak heights between several and tens of nanometers with the average between 20−30 nm. Furthermore, Ex-MMT was confirmed by XRD (Figure 2c). XRD patterns for pristine MMT in Milli-Q water and in dry conditions (control sample) were compared to Ex-MMT in Milli-Q water. For dry pristine MMT, the characteristic peaks at $2\theta$ of 7.4 (001), 19.8 (111), 26.7 (103), 28.5 (004), 35.4 (211) and 67.9° (342) were in good agreement with the reference MMT peaks (JCPDS card no. 60-0315). The basal plane (001) peak corresponds to an interlayer spacing of ∼1.20 nm, in good agreement with literature data.[29] When dispersed in Milli-Q water, the basal plane (001) peak of pristine MMT was broadened in the region of $2\theta = 5.7°$, corresponding to an interlayer spacing of 1.54 nm and signifying a slight swelling of the clay structure. For Ex-MMT, a complete loss of the (001) basal plane peak was observed, confirming the loss of the ordered stacking of clay platelets. The broad peaks observed in the $2\theta$ range of 20−30° are characteristic of an amorphous phase and/or water,[26] supporting the exfoliation of MMT.

Ex-MMT nanosheets were coated with polydopamine (PDOPA) to add catechol and amino groups that induce the assembly of Ex-MMT nanosheets, forming a hydrogel framework via a ligand−metal complexation mechanism.[23] The PDOPA-coated Ex-MMT nanosheets, named D-clay, were first mixed with $K_4Fe(CN)_6$ and reacted with a stoichiometric amount of $CuSO_4$, whereby potassium copper hexacyanoferrate (KCuHCF) nanoparticles were formed in situ. After this step, the product, named DHG(Cu-eq), had a slurry-like appearance (Figure 1), and was strongly cross-linked by the addition of extra $Cu^{2+}$ (0.4 mL of 1 M $CuSO_4$), via enhanced $Cu^{2+}$−ligand complexation, forming the composite hydrogel, DHG(Cu). The three-step fabrication route to form the composite hydrogel DHG(Cu) from Ex-MMT, and the sample appearance at each step in the fabrication method is shown in Figure 1.

FTIR spectroscopy was used to verify the following: (i) the successful coating of PDOPA on Ex-MMT, (ii) the formation of coordination bonds between D-clay nanosheets and $Cu^{2+}$

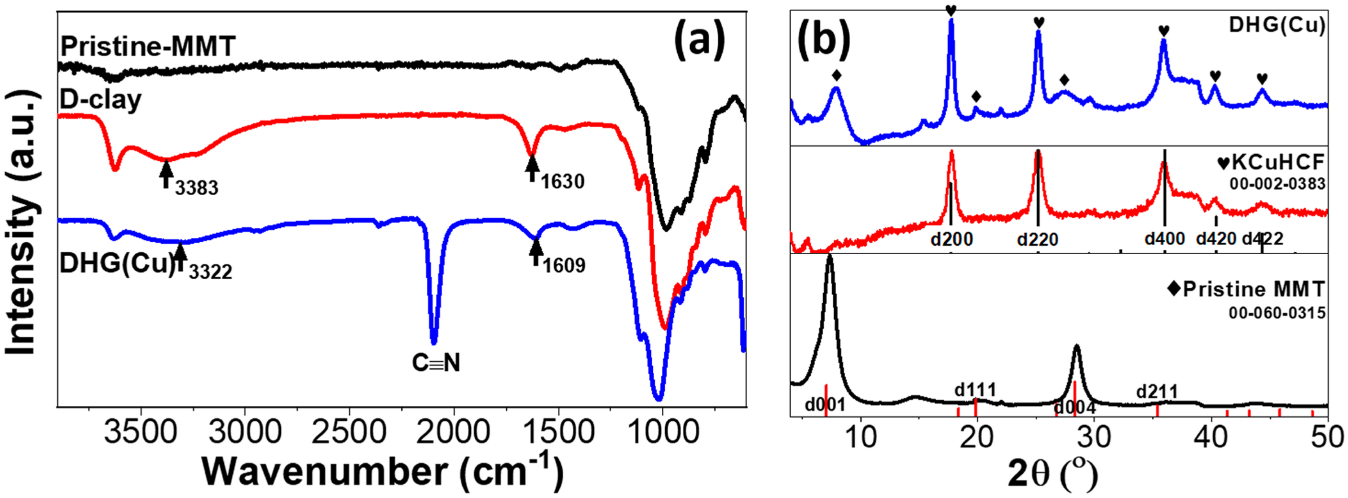

**Figure 3.** (a) FTIR spectra of pristine MMT, D-clay, and DHG(Cu). (b) PXRD patterns of DHG(Cu) and pristine MMT. The pattern files of pristine MMT (JCPDS-ICDD00-060-0315) and KCuHCF (JCPDS-ICDD00-002-0383) are presented as references.

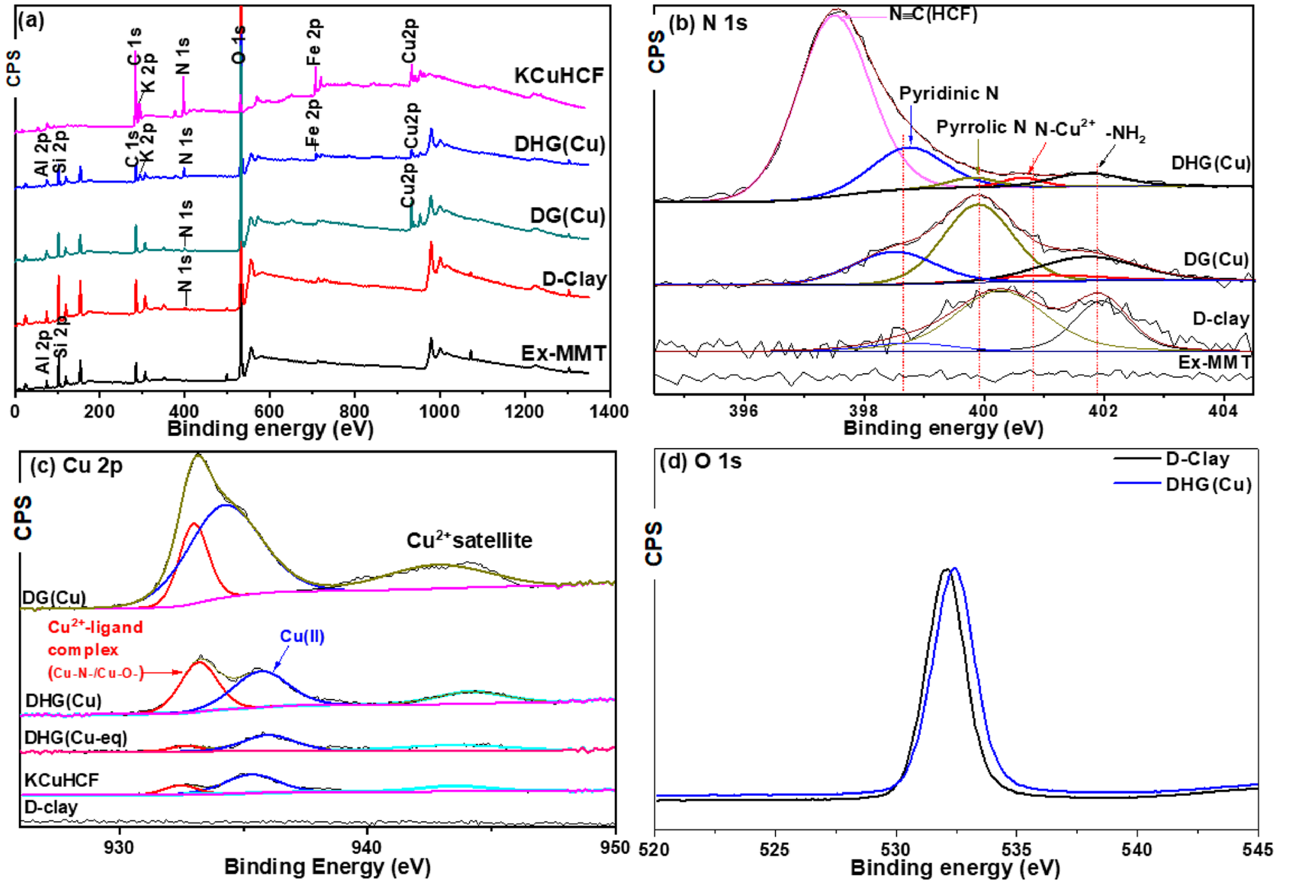

**Figure 4.** (a) XPS survey spectra of D-clay, DG(Cu), and DHG(Cu) with Ex-MMT and KCuHCF shown as references. (b) High-resolution XPS spectra of N 1s peaks of D-clay, DG(Cu), and DHG(Cu) with Ex-MMT as a reference (dashed line is used as a guide to the eye). (c) High-resolution XPS spectra of Cu 2p peaks of D-clay, KCuHCF, DHG(Cu-eq), DHG(Cu), and DG(Cu). (d) High-resolution XPS spectra of O 1s peaks of DHG(Cu) and D-clay.

ions; and (iii) the successful synthesis of KCuHCF nanoparticles. Figure 3a compares FTIR spectra of pristine MMT, D-clay, and DHG(Cu). Compared to pristine MMT, new peaks/bands emerged for D-clay, including a broad adsorption band in the range of 3100–3500 $cm^{-1}$ (consistent with the abundant surface hydroxyl groups) and a peak at 1630 $cm^{-1}$ (attributed to the stretching vibration of aromatic rings), which are both characteristics of PDOPA,[35,36] confirming the successful coating of PDOPA on Ex-MMT. Compared to D-clay, for the DHG(Cu) composite hydrogel, a noticeable shift in the broad adsorption band of hydroxyl groups (from 3383 to 3322 $cm^{-1}$) and the stretching vibration of aromatic rings (from 1630 to 1609 $cm^{-1}$) likely resulted from the interaction between $Cu^{2+}$ and ligands (e.g., aminol or catechol groups), affecting the stretching vibration of adjacent aromatic rings.[26] Also, the peak at ~1100 $\text{cm}^{-1}$, corresponding to the Si−O vibration of the tetrahedral silica sheet in MMT, was observed to shift to higher wavenumbers after the coating and complexation. The comparison of FTIR spectra validated our hypothesis of coordination bonds between the ligand and $Cu^{2+}$ being responsible for gelation. Moreover, for the DHG(Cu) hydrogel, a new peak emerged at 2073 $\text{cm}^{-1}$, which corresponds to the stretching vibration of CN,[3,34,37] confirming the formation of ferrocyanide (HCF) and the successful inclusion of KCuHCF nanoparticles within the hydrogel.

Powder X-ray diffraction (PXRD) patterns of DHG(Cu), KCuHCF, and pristine MMT are shown in Figure 3b. The characteristic diffraction peaks of pristine MMT at $2\theta$ of 7.4 (001), 19.9 (111), and 28.5° (004) (JCPDS card no. 60-0315) are evident, along with emerging peaks in DHG(Cu) at $2\theta$ of 17.9, 25.3, 36.1, 44.4, and 44.3°, which are assigned to the (200), (220), (400), (420), and (422) planes, respectively, of the cubic crystal structure of KCuHCF (JCPDS card No. 02-0383). The PXRD data further supports the incorporation of KCuHCF nanoparticles into the hydrogel. Moreover, the KCuHCF nanoparticle size can be approximated using the Scherrer equation:

$$L = \frac{K\lambda}{\beta \cos \theta} \tag{2}$$

where $K$ is a dimensionless factor for the crystal shape, taken to be 0.94;[3] $\lambda$ is the X-ray wavelength (1.5406 Å for Cu K$\alpha$); $\theta$ is the diffraction angle at the peak (rad); and $\beta$ is the full-width at half-maximum height (fwhm, rad). Using the major peaks at 17.9, 25.3, and 36.1°, the average particle size of KCuHCF in DHG(Cu) is 17.1 nm, consistent with previous research.[1,15,34]

To further confirm the fabrication route, XPS was conducted on D-clay, DG(Cu), and DHG(Cu) with Ex-MMT and KCuHCF included as references (Figure 4). The survey spectra indicated the emergence of the N 1s peak after coating PDOPA on Ex-MMT. In comparison to D-clay, the survey spectra clearly showed the presence of K 2p, Fe 2p, and Cu 2p peaks and an increased N 1s peak intensity for the composite hydrogel DHG(Cu), confirming the formation of KCuHCF. It is worth noting the Cu 2p peak originated not only from KCuHCF nanoparticles but also from the cross-linker used to assemble the Ex-MMT nanosheets into a gel. The $Cu^{2+}$cross-linker in DG(Cu) was confirmed by the clear Cu 2p peak. However, it is difficult to differentiate between the contributions from the $Cu^{2+}$ cross-linker and KCuHCF nanoparticles on the Cu content, since both contribute to the same peak as a result of the $Cu^{2+}$−ligand complex.

To reveal the potential coordination mechanisms of $Cu^{2+}$ and PDOPA to assemble the clay nanosheets, chemical bonds were analyzed based on high-resolution XPS (HRXPS) spectra of N 1s, Cu 2p, and O 1s (Figures 4b, c, and d, respectively). Deconvolution of the N 1s peak (Figure 4b) revealed the presence of three major components in D-clay, DG(Cu), and DHG(Cu), including pyridinic N (−N═C−, 398.76 eV), pyrrolic N (R−NH−R or indole groups, 400.28 eV),[38] and primary amine or its protonated form, i.e., nitrogen ($R{-}NH_2$/$R{-}NH_3^+$, 401.96 eV).[39] The presence of pyridinic N and pyrrolic N confirmed the self-polymerization of dopamine to PDOPA, which includes several different N-based bonding configurations as shown in Figure 1. The presence of the primary amine is thought to be the coexistence of non-covalently self-assembled dopamine in the covalent polymerized PDOPA.[27] Apart from the three components in both DG(Cu) and DHG(Cu), an additional peak at 400.5 eV was observed and corresponds to the chelation of amine groups with $Cu^{2+}$ ions[1] (Figure 1), contributing to the assembly of Ex-MMT nanosheets to form the gel network as well as the immobilization of KCuHCF nanoparticles on D-clay in DHG(Cu). The coordination between $Cu^{2+}$ and PDOPA on D-clay and the coordination between $Cu^{2+}$ and cyano group from KHCF, forming the KCuHCF nanoparticles, are likely to occur simultaneously on a single copper ion. This is due to the Cu−amine complex having a slightly distorted octahedral geometry with one of the amine ligands being labile[40] and can be displaced by the cyano group from the ferrocyanide anion of KHCF, see Figure 1. Hence, the nanoparticles are bound to the D-clay surface.

Moreover, deconvolution of the N 1s peak of DHG(Cu) revealed a strong peak at 397.5 eV (Figure 4b), assigned to the CN group ($[Fe(CN)_6]^{4-}$), signifying the presence of KCuHCF nanoparticles in the composite hydrogel (DHG(Cu)). From the component deconvolution of the N 1s peak, the $Cu^{2+}$−amine chelation was confirmed to be one of the complexation mechanisms of the Ex-MMT assembly to form the gel network. In fact, in mussel byssus the most significant complexation is between ferric and catechol in PDOPA.[42] To reveal whether metal ($Cu^{2+}$, in the current study)−catechol complexation (Figure 1) also exists and contributes to the formation of the gel network, the O 1s peak was compared between D-clay and DHG(Cu) (Figure 4d). The binding energy increment observed in the DHG(Cu) indicates the likely existence of the $Cu^{2+}$−catechol complexation.[43] The copper(II)−ligands (amino and catechol) chelation in DHG(Cu) was verified from the Cu $2p^{3/2}$ spectrum in Figure 4c, with a clear peak observed at ~932 eV, characteristic of Cu(I) as a result of the redox reaction of chelated $Cu^{2+}$ with amino and catechol groups.[41] This is also verified from the DG(Cu) sample with no KCuHCF, excluding the effect of the $Cu^{2+}{-}N{\equiv}C$ group in KCuHCF molecules. With the chelation of $Cu^{2+}$−ligands from the D-clay and $Cu^{2+}{-}N{\equiv}C$ group in the KCuHCF molecular structure (Figure 1), the peak intensity in DHG(Cu) was more significant than pure KCuHCF, where $Cu^{2+}{-}N{\equiv}C$ chelation occurs only in the KCuHCF molecular structure. As shown in Figure 4c, in cases when there is/are no/few $Cu^{2+}$−PDOPA complex(s) (i.e., KCuHCF and DHG(Cu-eq)), the peak has a relatively weaker intensity, while in cases when the $Cu^{2+}$−PDOPA complex is present (i.e., DHG(Cu)) or even dominant (i.e., DG(Cu)), the peak has a relatively stronger intensity, that is, the $Cu^{2+}$−PDOPA complex greatly contributes to the peak intensity.

TGA was used to approximate the mass of PDOPA coated on D-clay as well as the organic and KCuHCF fractions in DHG(Cu). As shown in Figure S4, both pure (Ex-MMT, KCuHCF, and PDOPA) and composite (D-clay and DHG(Cu)) components showed different decomposition levels over the temperature range of 30 to 900 °C. In particular, the small and gradual mass loss of Ex-MMT at ~700 °C is attributed to the dehydroxylation of the aluminum−silicate layer.[28] For KCuHCF, the mass loss at 250 °C is associated with the decomposition of the cyano group and elimination of the coordinating water, and the mass loss at 770 °C is due to the oxidative decomposition to iron oxides.[42] For PDOPA, the mass loss at 900 °C was ~52.0 wt %, which confirmed its good thermal stability as an organic component due to the carbon-yielding characteristic as a result of the structural similarity with the phenolic resin.[43,44] At 900 °C, residual mass (wt %) of D-clay was lower than Ex-MMT, a consequence of PDOPA degradation which was estimated to be ~5.00 wt % on D-clay.

The two characteristic decomposition temperatures of KCuHCF were observed in DHG(Cu); however, the temperatures were shifted to lower values, ca. 100 °C shift, which may result from the uniform dispersion of KCuHCF nanoparticles in DHG(Cu) compared to aggregated particles in bulk. The mass of KCuHCF in DHG(Cu) was estimated to be 84.5 wt %, based on the composite consisting of D-clay, KCuHCF, and $Cu^{2+}$ added in the second step as the cross-linker (see Supporting Information for the detailed calculation). A high incorporation of KCuHCF in the hydrogel was confirmed. The organic content of DHG(Cu) was ~0.64 wt %, confirming the majority of DHG(Cu) to be inorganic content.

ICP-OES was used to determine the metal content in DHG(Cu) based on Ex-MMT as a control sample (Table 1).

**Table 1. Metal Content of Ex-MMT and DHG(Cu) Determined by ICP-OES**

| sample | Cu (mmol/g) | Fe (mmol/g) | K (mmol/g) | Na (mmol/g) |
|---|---|---|---|---|
| Ex-MMT | 0.0002 | 0.4337 | 0.0010 | 0.5335 |
| DHG(Cu) | 2.2736 | 1.5778 | 0.7088 | 0.0096 |

The K/Fe molar ratio in DHG(Cu), with the Fe fraction determined by subtracting Ex-MMT, and the Cu/Fe molar ratio, based on the Cu content minus the fraction of $Cu^{2+}$ that was added in the second step as a cross-linker (i.e., 0.423 mmol/g, see the TGA analysis in Supporting Information), were used to propose an "equivalent" structure for the complex of KCuHCF, taking into account the possibility that several complexes with different compositions coexist. The form of KCuHCF incorporated in DHG(Cu) was estimated to be $K_{0.62}Cu_{1.62}[Fe(CN)_6]$, consistent with the published structure.[15]

The hydrogel morphologies of (i) DHG(Cu), (ii) DHG-(Fe), and (iii) DG(Cu), which was included as a control sample, were studied by cryo-SEM with the corresponding EDX elemental maps shown in Figure 5. All hydrogels showed a well-defined porous network, with layers of Ex-MMT stabilizing the micron-sized pores, confirmed by the clear traces of Si and Al elements (Figure 5b). The stabilization is mainly achieved by cross-linking between $Cu^{2+}$ and polydopamine (PDOPA) coated on the Ex-MMT, assembling the Ex-MMT nanosheets into a 3D network structure. While the initial addition of $Cu^{2+}$ can induce some degree of structuring, most of the $Cu^{2+}$ appears to be consumed in the synthesis of KCuHCF nanoparticles. For DHG(Cu) and DHG(Fe), small nanoparticles were detected on the hydrogel framework and were confirmed to be HCF nanoparticles by the presence of Cu, K, and Fe elements in the EDX elemental maps (Figure S5), therefore validating the immobilization of HCF nanoparticles on the Ex-MMT surface. The size of the KCuHCF nanoparticle as viewed by the cryo-SEM image was consistent with the XRD analysis.

## 3.2. Hydrogel Rheology and HCF Nanoparticle Retention.

All composite hydrogels were found to be strongly elastic, $G' > G''$, and exhibited a yield point beyond a critical strain (for example, DHG(Cu) = 145% at $G' = G''$, Figure 6a). The frequency-dependent data (Figure 6b) revealed DG(Cu) to be most strongly elastic ($G' \approx 6000$ Pa), with $G'$ decreasing in the order DHG(Fe) to DHG(Cu) and with $G'$ of DHG(step-Cu), DHG(Cu-eq) and DHG(step-Fe) being almost an order of magnitude lower than DHG(Cu). The small difference between DHG(Cu) and DHG(Fe) confirmed that the complexation by $Cu^{2+}$ or $Fe^{3+}$ led to hydrogels of comparable mechanical properties; however, the presence of HCF nanoparticles weakened the hydrogel viscoelasticity in comparison to DG(Cu), which is consistent with the understanding that KCuHCF nanoparticles occupy ligand sites on D-clay, linked via $Cu^{2+}$–ligand complexation, and inhibited the assembly of Ex-MMT nanosheets. Moreover, the presence of HCF nanoparticles on Ex-MMT nanosheets can provide a steric barrier to nanosheets assembly, which is thought to be the reason why the viscoelasticity of composite hydrogels was observed to decrease with increasing HCF content (data shown in Figure S6).

For DHG(step-Cu) and DHG(step-Fe), $Cu^{2+}$ was added first to the D-clay to induce the assembly of Ex-MMT nanosheets via $Cu^{2+}$–ligand complexation, followed by the addition of $K_4Fe(CN)_6$ to synthesize HCF nanoparticles. This fabrication route led to a significantly lower viscoelasticity of DHG(step-Cu) and DHG(step-Fe) compared to DHG(Cu) and DHG(Fe), respectively, with the subsequent growth of HCF nanoparticles likely disrupting the preformed hydrogel network.

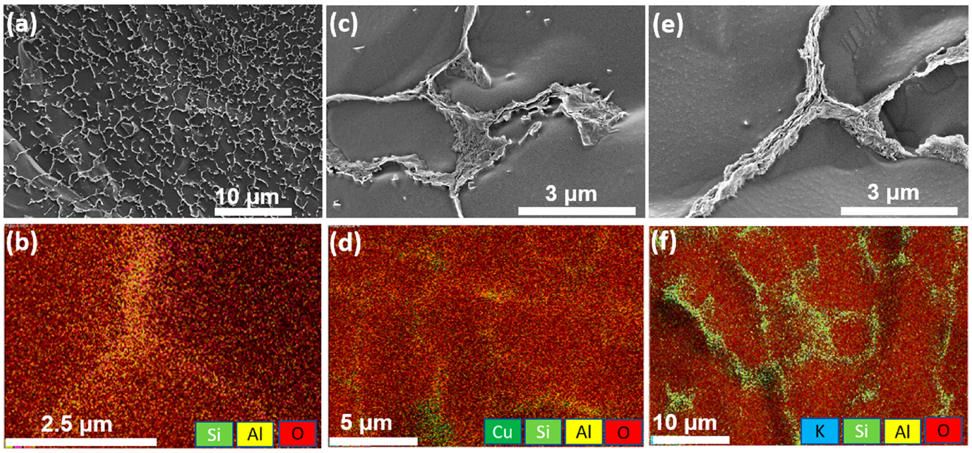

Figure 5. Cryo-SEM images and EDX elemental maps of the following: (a–b) DG(Cu), (c–d) DHG(Cu), and (e–f) DHG(Fe).

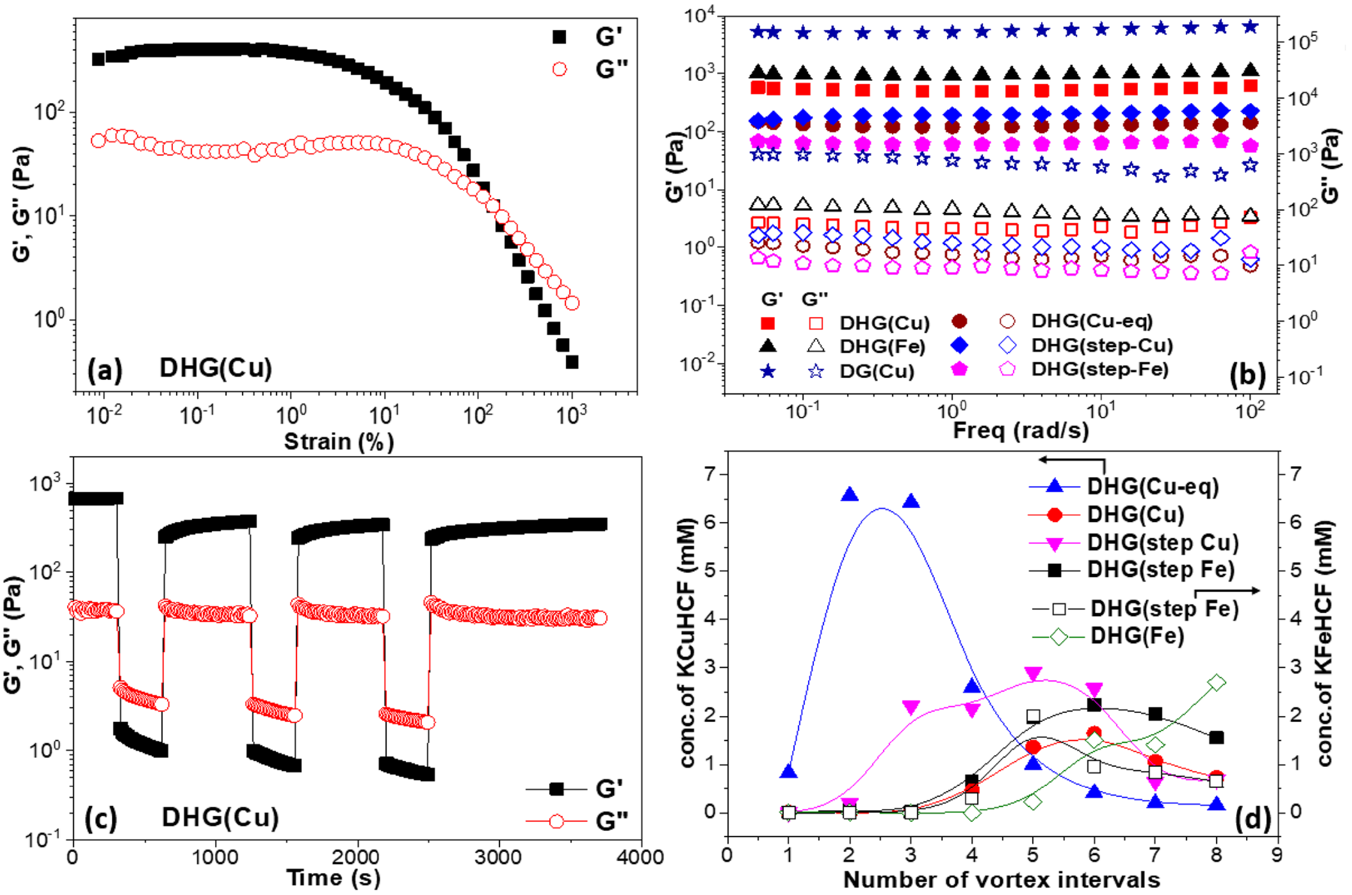

**Figure 6.** (a) $G'$ and $G''$ of DHG(Cu) undergoing a strain sweep test. (b) Frequency-dependent behavior of DHG(Cu), DHG(Fe), DG(Cu), DHG(Cu-eq), DHG(step-Cu), and DHG(step-Fe) at 1% strain. (c) Step-strain behavior of DHG(Cu) showing reversible recovery following sample yielding. (d) Concentration of KCuHCF and PB(KFeHCF) nanoparticles recovered from the supernatant following vigorous agitation in a vortex dispersion unit as a function of the number of vortex intervals.

A fascinating property of the complexation-induced hydrogel is its self-healing ability, which occurs by reforming ligand−metal complexes when the applied strain is below the critical yield point. Figure 6c shows a sequence of step strains above and below the critical yield point for DHG(Cu). Initially, a small strain, where $\gamma$ = 0.1% at $\omega$ = 1.0 rad/s, is applied to DHG(Cu) with $G' \approx 700$ Pa and $G'' \approx 40$ Pa; hence, the hydrogel is in a quasi-solid state. With increasing strain, where $\gamma$ = 1000% at $\omega$ = 1.0 rad/s, $G'$ decreases to ∼2 Pa and is below $G''$, signifying the hydrogel is now in a quasi-liquid state ($\tan \delta \equiv G''/G' \approx 1.5-2.5$). However, when the strain is decreased to $\gamma$ = 0.1% at $\omega$ = 1.0 rad/s, $G'$ recovers to ∼500 Pa (71% of the original value) and confirms the hydrogel recovers to a quasi-solid state ($\tan \delta \approx 0.04-0.07$). Subsequent strain-step increases and decreases demonstrate no significant loss in the viscoelasticity nor a change in the rate of structural reformation. This behavior demonstrates the robustness of the fabricated hydrogel to possible damage during sample handling/operation.

To assess the stability of HCF nanoparticles incorporated within the hydrogels, each sample was dispersed to form a suspension (fragmented hydrogel chunks) by vigorous vortex-shaking (intervals of 5 min), with the concentration of unbound HCF nanoparticles in the supernatant measured by UV spectroscopy. The hydrogel was repeatedly vortexed with fresh Milli-Q water and centrifuged with supernatants decanted. Figure 6d compares the concentration of HCF nanoparticles as a function of the hydrogel-type and number of vortex intervals. Poor HCF nanoparticle retention was seen for DHG(Cu-eq), the sample of the intermediate reactant without additional cross-linking, where most HCF nanoparticles were released during the first few vortex intervals.

However, for DHG(Cu) and DHG(Fe), hydrogels with a high cross-linking density, HCF nanoparticles remained undetected following the first three vortex intervals and confirmed the strong immobilization of the HCF nanoparticles. Subsequent vortex intervals resulted in low-levels of HCF nanoparticles being released into the supernatant. The ability of the hydrogel to retain HCF nanoparticles corresponded to increased elasticity, as measured by $G'$, see Figure 6b.

**3.3. Cesium Adsorption.** The adsorption ($q$, mg of adsorbate/g of adsorbent) of $Cs^+$ by the D-clay/HCF composite hydrogels was studied as a function of the equilibrium $Cs^+$ concentration ($C_e$, ppm) in solution. The well-known Langmuir model, which assumes (i) surface monolayer sorption, (ii) finite number of binding sites, (iii) uniform sorption energies, and (iv) no transmigration of sorbates in the plane of the surface, was used to describe the $Cs^+$ adsorption behavior. The Langmuir isotherm is given by

$$q = \frac{bq_m C_e}{1 + bC_e} \tag{3}$$

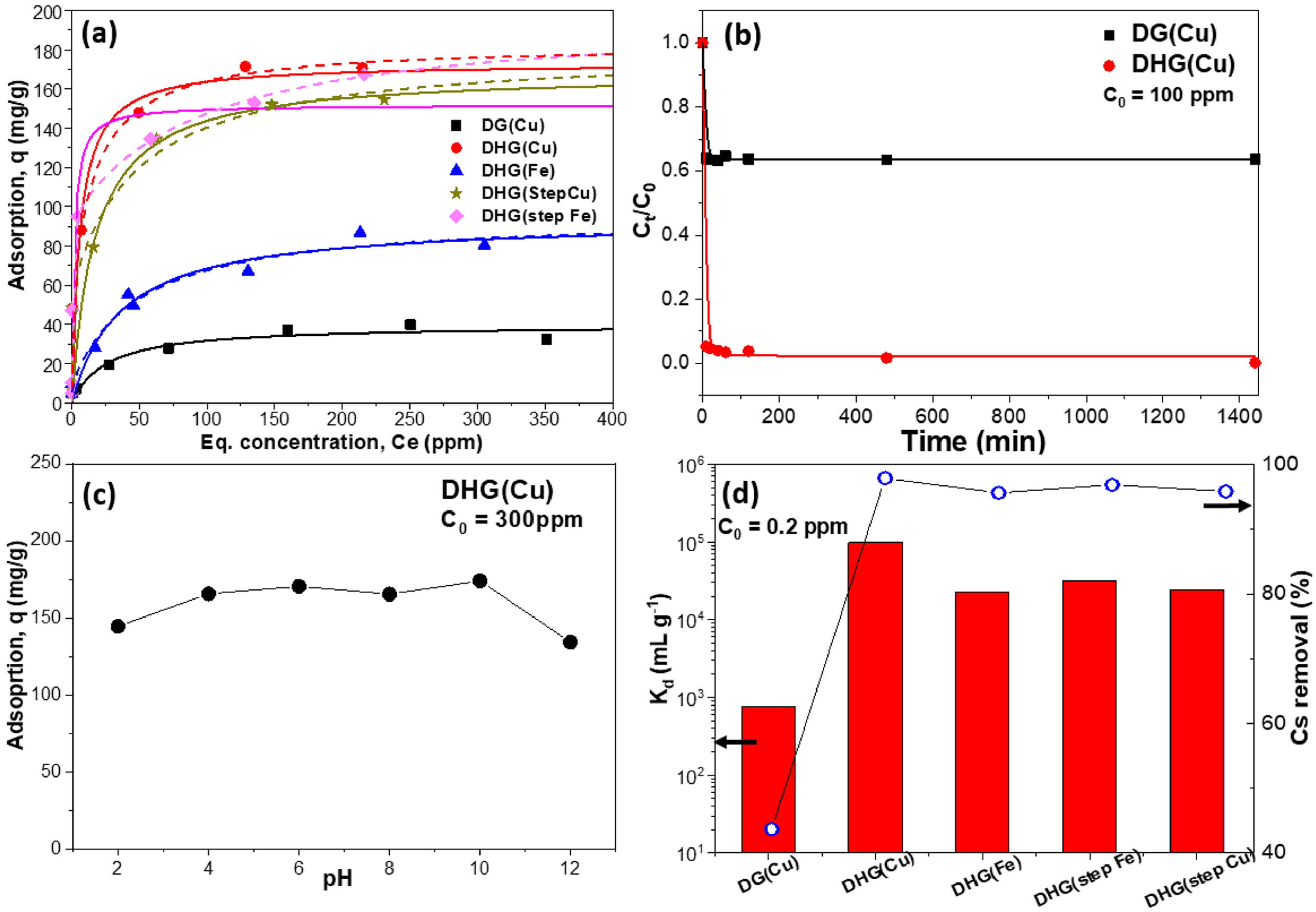

**Figure 7.** (a) $Cs^+$ adsorption as a function of the equilibrium concentration ($C_e$) for D-clay/HCF composite hydrogels, with DG(Cu) included as a reference. Solid and dashed lines represent single-site and dual-site Langmuir models, respectively. (b) $Cs^+$ adsorption kinetics by DHG(Cu) and DG(Cu) at $C_0$ = 100 ppm. (c) $Cs^+$ adsorption by DHG(Cu) as a function of the solution pH ($C_0$ = 300 ppm). (d) Distribution coefficient $K_d$ and removal efficiency of $Cs^+$ from seawater ($C_0$ = 0.2 ppm) by D-clay/HCF composite hydrogels, with DG(Cu) included as a reference.

**Table 2. Single-Site and Dual-Site Langmuir Isotherm Models for $Cs^+$ Adsorption**

| | Langmuir | | | dual-site Langmuir | | | | |
|---|---|---|---|---|---|---|---|---|
| sample | $q_m$ (mg/g) | $b$ (L/mg) | $R^2$ | $q_{m1}$ (mg/g) | $b_1$ (L/mg) | $q_{m2}$ (mg/g) | $b_2$ (L/mg) | $R^2$ |
| DG(Cu) | 39.7 | 0.039 | 0.910 | | | | | |
| DHG(Cu) | 173.3 | 0.170 | 0.934 | 136.6 | 0.062 | 46.5 | 127.089 | 0.998 |
| DHG(Fe) | 93.2 | 0.028 | 0.958 | 86.7 | 0.021 | 9.0 | 91.700 | 0.963 |
| DHG(step Cu) | 168.6 | 0.058 | 0.927 | 123.2 | 0.021 | 56.9 | 57.071 | 0.957 |
| DHG(step Fe) | 152.0 | 0.579 | 0.927 | 103.3 | 0.010 | 94.9 | 4.469 | 0.999 |

where $b$ is the Langmuir constant related to the affinity coefficient of binding sites (L/mg) and $q_m$ is the maximum sorption capacity of $Cs^+$.

As shown in Figure 7a, the experimental data was well-fitted by the Langmuir isotherm. The Langmuir fitting parameters, $q_m$ and $b$, and the associated correlation coefficient ($R^2$) values for each hydrogel are provided in Table 2. In comparison to the low adsorption capacity of DG(Cu), $q_m \approx 39.7$ mg/g, the D-clay/HCF composite hydrogels showed significantly enhanced $q_m$ values, particularly DHG(Cu), which had the highest adsorption capacity of 173.3 mg/g, and confirmed the successful inclusion of KCuHCF nanoparticles into the inorganic−organic hydrogel.

Considering there is more than one sorption site with different sorption energies in the D-clay/HCF composite hydrogel, such as binding sites from D-clay and KCuHCF nanoparticles, the dual-site Langmuir adsorption model was considered to better describe sorption behavior:

$$q = \frac{b_1 q_{m1} C_e}{1 + b_1 C_e} + \frac{b_2 q_{m2} C_e}{1 + b_2 C_e} \qquad (4)$$

where the fitting parameters $b_1$ and $b_2$, and $q_{m1}$ and $q_{m2}$ represent the affinity coefficients (L/mg) and the maximum sorption capacity (mg/g) for the two types of sorption sites, respectively. As shown in Figure 7a and Table 2, the dual-site Langmuir model provided a better description of the adsorption behavior for the D-clay/HCF composite hydrogels, with higher $R^2$ values reported. While HCF nanoparticles (KCuHCF/KFeHCF) are strong (abundant) binding sites, the D-clay (DG(Cu)) also provides some binding sites for $Cs^+$ but

**Table 3. Summary of Hydrogel-Based Composites Used to Recover $Cs^+$. Material Performance Compared by Capacity ($q_m$) and Time to Reach Equilibrium (Eq. Time)**

| adsorbent | hydrogel support | $q_m$ (mg of Cs/g of composite) | pH | eq. time | ref /year |
|---|---|---|---|---|---|
| KCuHCF | cellulose | 309.0 | 6.0 | >99% after 4 h | Kim et al.[34] /2017 |
| benzo-18-crown-6(B18C6) | polyacrylic acid (PAAc) | 74.6 | 6.0 | ∼200 min ($C_0$ = 2 mM) | Yu et al.[42] /2017 |
| ammonium molybdophosphate | poly(vinyl alcohol)-sodium alginate (PVA-SA) | 71.3 | 7.0 | ∼12 h ($C_0$ = 50 ppm) | Chen et al.[45] /2019 |
| KNiHCF | PVA-SA | 64.0 | 7.0 | ∼60 min ($C_0$ = 20 ppm) | Dwivedi et al.[46] /2015 |
| KCuHCF | PVA-citric acid | 82.8 | 6.0 | 90% in 3 h ($C_0$ = 8 ppm) | Kim et al.[20] /2017 |
| copper ferrocyanide | PVA | 17.4 | 7.0 | >10 h | Lee et al.[47]/2019 |
| TEMPO system | cellulose | 133.8 | 5.0−6.0 | | Isobe et al.[48] /2013 |
| KCuHCF | magnetic PVA | 82.8 | 7.0 | ∼400 min ($C_0$ = 8 ppm) | Kim et al.[20] /2017 |
| KCuHCF | montmorillonite | 173.3 | 6.0 | ∼100 min ($C_0$ = 100 ppm) | current study |

comparatively less (shown by comparing DG(Cu) and DHG(Cu)), with the likely binding sites being Ex-MMT.

Table 3 provides a summary of recently reported hydrogel-based composite adsorbents used to recover Cs. As shown, the newly fabricated DHG(Cu) adsorbent provides some of the best performance properties, which can be attributed to the successful incorporation of dispersed KCuHCF nanoparticles within the mostly inorganic membrane, providing multiple binding sites for $Cs^+$.

*3.3.1. Adsorption Kinetics.* $Cs^+$ adsorption kinetics were studied for DG(Cu) and DHG(Cu) (Figure 7b). As shown, $Cs^+$ adsorption by both hydrogels was reasonably fast, reaching equilibrium (i.e., $C_t/C_0$ = constant) within 30 and 100 min for DG(Cu) and DHG(Cu), respectively. To quantitatively describe the adsorption kinetics, the experimental data were fitted using a pseudo-second order rate equation (PSORE):

$$\frac{t}{q_t} = \frac{1}{k_2 {q_e}^2} + \frac{t}{q_e} \tag{5}$$

where $q_t$ is the adsorbed $Cs^+$ quantity (mg/g) at time $t$, $q_e$ is the adsorbed $Cs^+$ quantity (mg/g) at equilibrium, and $k_2$ is a rate constant.

For both DG(Cu) and DHG(Cu), the PSORE fits were very good with $R^2$ values >0.99. The fitting parameters are shown in Table 4. For comparison, the values for bulk KCuHCF reported in our earlier study[34] have also been included in Table 4. Although the rate constant, $k_2$, for DHG(Cu) was lower than DG(Cu), the total $Cs^+$ uptake by DHG(Cu) was much greater and exceeded 80% within 30 min, compared to less than 30% by DG(Cu) under the same experimental conditions ($C_0$ = 100 ppm). Compared to bulk KCuHCF, DHG(Cu) exhibited faster kinetics but was found to be intermediate of DH(Cu) (fastest kinetics) and KCuHCF (slowest kinetics), in good agreement with the performance characteristics of other composite materials such as chitin beads[15] and cellulose hydrogels[34] used as KCuHCF supports.

**Table 4. Pseudo-Second Order Rate Equation Fitting Parameters for $Cs^+$ Adsorption by DH(Cu) and DHG(Cu)**

| sample | $k_2$ (g/(mg min)) | $q_e$ (mg/g) | $R^2$ |
|---|---|---|---|
| DH(Cu) | 0.5992 | 34.06 | 0.9986 |
| DHG(Cu) | 0.0251 | 97.84 | 0.9988 |
| bulk KCuHCF (19.9 ppm $Cs^+$ in DI water)[34] | $4.3943 \times 10^{-4}$ | 94.37 | 0.9864 |

*3.3.2. pH Effect.* The effect of pH on $Cs^+$ adsorption by DHG(Cu) (selected due to its high $Cs^+$ adsorption capacity) is shown in Figure 7c. DHG(Cu) showed very good removal of $Cs^+$ over a wide pH range, with a small variation around the mean ($q_m$ = 159 mg/g) of 16 mg/g. A slight decrease in the adsorption capacity was observed at pH 2 (144 mg/g) and 12 (134 mg/g), which for the strongly acidic condition is likely to result from competition between $Cs^+$ and $H^+$ for the available sorption sites, as well as the possible decomposition of the Prussian blue (PB) structure.[37] The reduced performance at very high pH values is attributed to the instability of PDOPA under strong alkaline conditions,[45] leading to the reduced cross-linking of the hydrogel and release of KCuHCF nanoparticles into the supernatant (observed by the increased reddish-brown color of the supernatant at high pH values). As such, those measurements of the $Cs^+$ concentration will be compromised since the unbound KCuHCF nanoparticles cannot be filtered from the supernatant prior to measuring by ICP-MS.

*3.3.3. Competitive Ion Effect.* The $Cs^+$ removal performance by the fabricated hydrogels was studied in more realistic conditions with 0.2 ppm $Cs^+$ added to seawater, $Cs^+$ selectivity is described by the distribution coefficient, $K_d$:

$$K_d = \frac{(C_0 - C_e)}{C_e}\frac{V}{m} \tag{6}$$

where $C_0$ and $C_e$ are the initial and equilibrium concentrations of $Cs^+$, $V$ is the volume (mL) of the solution, and $m$ is the mass (g) of sorbent. Using eq 6, DG(Cu) showed relatively poor $Cs^+$ selectivity, $K_d = 7.75 \times 10^2$ mL/g, with less than 45% $Cs^+$ recovered, while the D-clay/HCF composite hydrogels showed very high $Cs^+$ selectivity, with $K_d$ values for DHG(Cu), DHG(Fe), DHG(step-Fe), and DHG(step-Cu) of $9.78 \times 10^4$, $2.26 \times 10^4$, $3.19 \times 10^4$, and $2.38 \times 10^4$ mL/g, respectively, and all with removal efficiencies greater than 95%, see Figure 7d. Such high selectivities demonstrates the fabricated hydrogels are suitably robust to work in challenging environments and remove minor quantities of $Cs^+$ from complex ionic backgrounds.

Poor selectivity is often a limitation of unmodified inorganic species such as clays, with selectivity values ranging from ∼10−$10^3$ mL/g.[33,49] The enhanced performance of D-clay/HCF composite hydrogels, particularly DHG(Cu), is attributed to the the well-dispersed incorporation of HCF nanoparticles in the inorganic−organic matrix, where the cubic structure of HCF acts as an ion sieve, selectively removing hydrated $Cs^+$

(0.329 nm) while blocking the infiltration of larger hydrated ions such as $Na^+$ (0.358 nm), $K^+$ (0.331 nm), $Mg^{2+}$ (0.428 nm),[5] and $Ca^{2+}$(0.420 nm).[50]

*3.3.4. Filtration tests.* A simple purification test was conducted by filtering 20 mL of contaminated water ($Cs^+$, $C_0$ = 0.5 ppm in Milli-Q water and seawater) through the DHG(Cu) hydrogel of increasing mass (0.5−6 g, see Figure 8). The DHG(Cu) hydrogel was selected for column filtration tests as it offered superior rheological properties (Figures 6b−c), providing good mechanical properties and a strong retention of KCuHCF nanoparticles within the hydrogel (Figure 6d), ensuring the optimal removal capacity for $Cs^+$. As shown in Figure 8, the DHG(Cu) hydrogel showed an excellent performance when filtering both Cs-doped Milli-Q water and Cs-doped seawater. A slight reduction in the performance (~93% $Cs^+$ recovered) was measured when filtering Cs-doped seawater through 0.5 g of DHG(Cu). On the basis of the batch adsorption tests, where $K_d = 9.78 \times 10^4$ mL/g for DHG(Cu) in seawater, the removal of $Cs^+$ ($C_0$ = 0.5 ppm) by 0.5 g of the wet hydrogel (water content 97.3 wt %) is estimated to be 99.96% (batch removal). Therefore, the small decrease in $Cs^+$ removal by 0.5 g of DHG(Cu) likely resulted from the short residence time of the filtered liquid in the membrane, with the performance limited by adsorption kinetics (Figure 7b). Moreover, to evaluate the purification volume capacity of the hydrogel membrane, the breakthrough volume ($b_v$) was approximated using the following equation:[51]

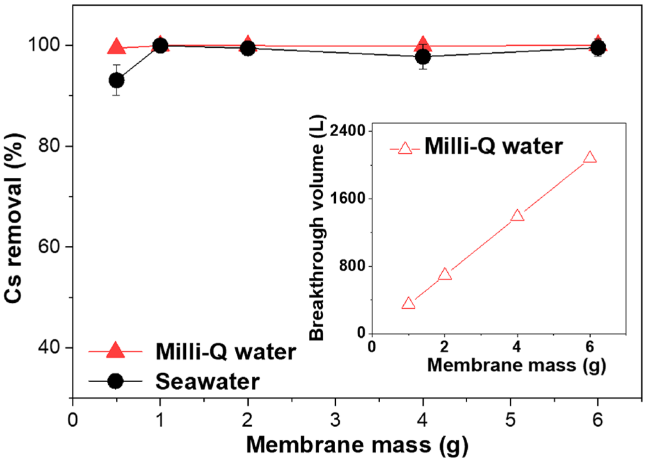

**Figure 8.** $Cs^+$ removal (%) from 20 mL of Cs-doped (0.5 ppm) Milli-Q water or seawater as a function of DHG(Cu) membrane mass. Inset shows the breakthrough volume versus the membrane mass for Cs-contaminated Milli-Q water.

$$b_v = q_b / \left[\frac{C_i - C_b}{m}\right] \quad (7)$$

where $C_i$ and $C_b$ are the initial and breakthrough concentrations (ppm) of $Cs^+$, respectively; $q_b$ is the breakthrough adsorption capacity, taken to be the maximum adsorption capacity of 173 mg/g (Table 2 for DHG(Cu)); and $m$ is the mass of the adsorbent (g). As shown in the inset of Figure 8, the volume of Cs-doped (0.5 ppm) Milli-Q water to be purified by the hydrogel membrane increased from 346 L for 1.0 g of DHG(Cu) to more than 2000 L for 6 g of DHG(Cu) membrane used.

The regeneration of the composite adsorbent was not considered in the current study. The most appropriate method to regenerate the transition metal hexacyanoferrate (HCF) is through acid washing. However, the use of nitric acid has been shown to only partially regenerate HCF,[52] and strong acids can lead to the degradation of the HCF and PDOPA.

## 4. CONCLUSIONS

A clay-based hexacyanoferrate composite hydrogel, DHG(Cu), with a low organic content (~0.64 wt %) was successfully fabricated via a bio-inspired route to recover $Cs^+$ from contaminated water. Membrane fabrication involved 3-steps following the exfoliation of montmorillonite (Ex-MMT): step 1, coating a thin layer of polydopamine (PDOPA) onto Ex-MMT to form D-clay; step 2, mixing D-clay with the hexacyanoferrate (HCF) precursor, followed by the equimolar addition of $Cu^{2+}$ to synthesize and immobilize HCF nanoparticles; step 3, enhanced self-assembly of the composite hydrogel with additional $Cu^{2+}$. The fabrication route was verified by FTIR and XPS analysis, with the mechanism for HCF immobilization and self-assembly of clay nanosheets occurring via a copper−ligand complexation.

Cryo-SEM images revealed that the composite hydrogel was a cross-linked structure of exfoliated clay nanosheets with KCuHCF nanoparticles located along the skeletal structure of the hydrogel. The composite hydrogel was found to be elastic, with the elasticity able to recover (self-healing) following structural yielding, and the strong structural integrity of the hydrogel leading to good retention of KCuHCF nanoparticles.

The composite hydrogel, DHG(Cu), showed an excellent recovery of $Cs^+$ from contaminated environments, with a maximum adsorption capacity in Milli-Q water of ~173 mg/g. $Cs^+$ adsorption occurred mostly by ion-exchange between $Cs^+$ and $K^+$ in the cubic lattice of KCuHCF, while the D-clay also provided some potential to recover $Cs^+$ by electrostatic adsorption. The hydrogel membrane showed good performance over a wide pH range (pH 2−12), recovered low concentrations of $Cs^+$ from seawater, and could be easily shaped into a membrane to recover $Cs^+$ by column filtration. The study highlighted a simple route to fabricate mechanically robust membranes of very low organic contents and to successfully retain HCF nanoparticles within the structure to deliver an excellent $Cs^+$ removal performance, both properties highly desired for applications in radioactive environments.

## 5. DATA STATEMENT

Huagui Zhang, Chris S. Hodges, Prashant Kumar Mishra, Ji Young Yoon, Timothy N. Hunter, Jae W. Lee, and David Harbottle (2020): Data associated with 'Bio-Inspired Preparation of Clay−Hexacyanoferrate Composite Hydrogels as Super Adsorbents for $Cs^{+}$', University of Leeds. [Dataset]. https://doi.org/10.5518/838. Article metadata is available under a Creative Commons Attribution license (CC-BY).[53]

## ■ ASSOCIATED CONTENT

### Supporting Information

The Supporting Information is available free of charge at https://pubs.acs.org/doi/10.1021/acsami.0c06598.

Table S1: fabrication sequence for the different adsorbents tested. Figure S1: (a) schematic of the fabrication routes to prepare DHG(step-Cu), DHG(step-Fe), and DHG(Fe), and (b) images of DG(Cu), DHG(step-Cu), DHG(step-Fe), DHG(Cu), and DHG(Fe). Figure S2: UV−vis adsorption bands of KCuHCF and KFeHCF particle suspensions. Figure S3: SEM image of pristine MMT particles. Figure S4: TGA of Ex-MMT, D-clay, DHG(Cu), and pure KCuHCF and PDOPA. Figure S5: SEM image and EDX map of DHG(Cu). Figure S6: the effect of HCF content on the viscoelasticity of composite hydrogels (PDF)

## ■ AUTHOR INFORMATION

### Corresponding Authors

**David Harbottle** − *School of Chemical and Process Engineering, University of Leeds, Leeds LS2 9JT, United Kingdom;* orcid.org/0000-0002-0169-517X; Phone: +44 (0) 113 343 4154; Email: d.harbottle@leeds.ac.uk

**Huagui Zhang** − *School of Chemical and Process Engineering, University of Leeds, Leeds LS2 9JT, United Kingdom; College of Chemistry and Materials Science, Fujian Key Laboratory of Polymer Science, Fujian Normal University, Fuzhou 350007, China*; Email: huagui.zhang@fjnu.edu.cn

### Authors

**Chris S. Hodges** − *School of Chemical and Process Engineering, University of Leeds, Leeds LS2 9JT, United Kingdom*

**Prashant Kumar Mishra** − *School of Chemical and Process Engineering, University of Leeds, Leeds LS2 9JT, United Kingdom*

**Ji Young Yoon** − *Chemical and Biomolecular Engineering, Korean Advanced Institute of Science and Technology, Daejeon 305-732, The Republic of Korea*

**Timothy N. Hunter** − *School of Chemical and Process Engineering, University of Leeds, Leeds LS2 9JT, United Kingdom;* orcid.org/0000-0003-3922-491X

**Jae W. Lee** − *Chemical and Biomolecular Engineering, Korean Advanced Institute of Science and Technology, Daejeon 305-732, The Republic of Korea;* orcid.org/0000-0002-8756-0195

Complete contact information is available at:
https://pubs.acs.org/10.1021/acsami.0c06598

### Notes

The authors declare no competing financial interest.

## ■ ACKNOWLEDGMENTS

This work was financially supported by the Engineering and Physical Sciences Research Council (EPSRC) by Grants EP/M026426/1 (H.Z., T.N.H, and D.H) and EP/S032797/1 (P.K.M., T.N.H, and D.H.) and the National Research Foundation of Korea (NRF) by Grant NRF-2019M2A7A1001773 (J.W.L.). H.Z. acknowledges the National Natural Science Foundation of China (21903015) and the Fujian Minjiang Scholar Award Program. X-ray photoelectron spectra were performed at the EPSRC National Facility for XPS ("HarwellXPS"), operated by Cardiff University and UCL, under Contract No. PR16195.

## ■ REFERENCES

(1) Zhang, H.; Kim, Y. K.; Hunter, T. N.; Brown, A. P.; Lee, J. W.; Harbottle, D. Organically Modified Clay with Potassium Copper Hexacyanoferrate for Enhanced Cs+ Adsorption Capacity and Selective Recovery by Flotation. *J. Mater. Chem. A* **2017**, *5* (29), 15130−15143.

(2) Baik, S.; Zhang, H.; Kim, Y. K.; Harbottle, D.; Lee, J. W. Enhanced Adsorption Capacity and Selectivity Towards Strontium Ions in Aqueous Systems by Sulfonation of Co2 Derived Porous Carbon. *RSC Adv.* **2017**, *7* (86), 54546−54553.

(3) Turgis, R.; Arrachart, G.; Delchet, C.; Rey, C.; Barre, Y.; Pellet-Rostaing, S.; Guari, Y.; Larionova, J.; Grandjean, A. An Original "Click and Bind" Approach for Immobilizing Copper Hexacyanoferrate Nanoparticles on Mesoporous Silica. *Chem. Mater.* **2013**, *25* (21), 4447−4453.

(4) Awual, M. R.; Yaita, T.; Taguchi, T.; Shiwaku, H.; Suzuki, S.; Okamoto, Y. Selective Cesium Removal from Radioactive Liquid Waste by Crown Ether Immobilized New Class Conjugate Adsorbent. *J. Hazard. Mater.* **2014**, *278*, 227−235.

(5) Yang, S. B.; Okada, N.; Nagatsu, M. The Highly Effective Removal of Cs+ by Low Turbidity Chitosan-Grafted Magnetic Bentonite. *J. Hazard. Mater.* **2016**, *301*, 8−16.

(6) Kadam, A. A.; Jang, J.; Lee, D. S. Facile Synthesis of Pectin-Stabilized Magnetic Graphene Oxide Prussian Blue Nanocomposites for Selective Cesium Removal from Aqueous Solution. *Bioresour. Technol.* **2016**, *216*, 391−398.

(7) Yang, H. M.; Jang, S. C.; Hong, S. B.; Lee, K. W.; Roh, C.; Huh, Y. S.; Seo, B. K. Prussian Blue-Functionalized Magnetic Nanoclusters for the Removal of Radioactive Cesium from Water. *J. Alloys Compd.* **2016**, *657*, 387−393.

(8) Datta, S. J.; Moon, W. K.; Choi, D. Y.; Hwang, I. C.; Yoon, K. B. A Novel Vanadosilicate with Hexadeca-Coordinated Cs+ Ions as a Highly Effective Cs+ Remover. *Angew. Chem., Int. Ed.* **2014**, *53* (28), 7203−7208.

(9) Ding, N.; Kanatzidis, M. G. Selective Incarceration of Caesium Ions by Venus Flytrap Action of a Flexible Framework Sulfide. *Nat. Chem.* **2010**, *2* (3), 187−191.

(10) Borai, E. H.; Harjula, R.; Malinen, L.; Paajanen, A. Efficient Removal of Cesium from Low-Level Radioactive Liquid Waste Using Natural and Impregnated Zeolite Minerals. *J. Hazard. Mater.* **2009**, *172* (1), 416−422.

(11) Prajitno, M. Y.; Harbottle, D.; Hondow, N.; Zhang, H.; Hunter, T. N. The Effect of Pre-Activation and Milling on Improving Natural Clinoptilolite for Ion Exchange of Cesium and Strontium. *J. Environ. Chem. Eng.* **2020**, *8* (1), 102991.

(12) Ma, B.; Oh, S.; Shin, W. S.; Choi, S. J. Removal of Co2+, Sr2+ and Cs+ from Aqueous Solution by Phosphate-Modified Montmorillonite (Pmm). *Desalination* **2011**, *276* (1−3), 336−346.

(13) Gu, P. C.; Zhang, S.; Li, X.; Wang, X. X.; Wen, T.; Jehan, R.; Alsaedi, A.; Hayat, T.; Wang, X. K. Recent Advances in Layered Double Hydroxide-Based Nanomaterials for the Removal of Radionuclides from Aqueous Solution. *Environ. Pollut.* **2018**, *240*, 493−505.

(14) Delchet, C.; Tokarev, A.; Dumail, X.; Toquer, G.; Barre, Y.; Guari, Y.; Guerin, C.; Larionova, J.; Grandjean, A. Extraction of Radioactive Cesium Using Innovative Functionalized Porous Materials. *RSC Adv.* **2012**, *2* (13), 5707−5716.

(15) Vincent, T.; Vincent, C.; Barre, Y.; Guari, Y.; Le Saout, G.; Guibal, E. Immobilization of Metal Hexacyanoferrates in Chitin Beads for Cesium Sorption: Synthesis and Characterization. *J. Mater. Chem. A* **2014**, *2* (26), 10007−10021.

(16) Yang, H. J.; Li, H. Y.; Zhai, J. L.; Sun, L.; Zhao, Y.; Yu, H. W. Magnetic Prussian Blue/Graphene Oxide Nanocomposites Caged in Calcium Alginate Microbeads for Elimination of Cesium Ions from Water and Soil. *Chem. Eng. J.* **2014**, *246*, 10−19.

(17) Yang, H. J.; Li, H. Y.; Zhai, J. L.; Yu, H. W. In Situ Growth of Prussian Blue Nanocrystal within Fe3+ Crosslinking Paa Resin for Radiocesium Highly Efficient and Rapid Separation from Water. *Chem. Eng. J.* **2015**, *277*, 40−47.

(18) Yang, H. M.; Hwang, K. S.; Park, C. W.; Lee, K. W. Sodium-Copper Hexacyanoferrate-Functionalized Magnetic Nanoclusters for the Highly Efficient Magnetic Removal of Radioactive Caesium from Seawater. *Water Res.* **2017**, *125*, 81−90.

(19) Jang, S. C.; Haldorai, Y.; Lee, G. W.; Hwang, S. K.; Han, Y. K.; Roh, C.; Huh, Y. S. Porous Three-Dimensional Graphene Foam/

Prussian Blue Composite for Efficient Removal of Radioactive Cs-137. *Sci. Rep.* **2015**, *5* (1), 17510.

(20) Kim, Y. K.; Kim, T.; Kim, Y.; Harbottle, D.; Lee, J. W. Highly Effective Cs+ Removal by Turbidity-Free Potassium Copper Hexacyanoferrate-Immobilized Magnetic Hydrogels. *J. Hazard. Mater.* **2017**, *340*, 130−139.

(21) Mohapatra, P. K.; Raut, D. R.; Ghosh, A. K.; Reddy, A. V. R.; Manchanda, V. K. Radiation Stability of Several Polymeric Supports Used for Radionuclide Transport from Nuclear Wastes Using Liquid Membranes. *J. Radioanal. Nucl. Chem.* **2013**, *298* (2), 807−811.

(22) Zakrzewska-Trznadel, G. Advances in Membrane Technologies for the Treatment of Liquid Radioactive Waste. *Desalination* **2013**, *321*, 119−130.

(23) Lee, H.; Dellatore, S. M.; Miller, W. M.; Messersmith, P. B. Mussel-Inspired Surface Chemistry for Multifunctional Coatings. *Science* **2007**, *318* (5849), 426−430.

(24) Holten-Andersen, N.; Harrington, M. J.; Birkedal, H.; Lee, B. P.; Messersmith, P. B.; Lee, K. Y. C.; Waite, J. H. Ph-Induced Metal-Ligand Cross-Links Inspired by Mussel Yield Self-Healing Polymer Networks with near-Covalent Elastic Moduli. *Proc. Natl. Acad. Sci. U. S. A.* **2011**, *108* (7), 2651−2655.

(25) Li, Q.; Barrett, D. G.; Messersmith, P. B.; Holten-Andersen, N. Controlling Hydrogel Mechanics Via Bio-Inspired Polymer-Nanoparticle Bond Dynamics. *ACS Nano* **2016**, *10* (1), 1317−1324.

(26) Huang, S.; Yang, L. P.; Liu, M.; Phua, S. L.; Yee, W. A.; Liu, W. S.; Zhou, R.; Lu, X. H. Complexes of Polydopamine-Modified Clay and Ferric Ions as the Framework for Pollutant-Absorbing Supramolecular Hydrogels. *Langmuir* **2013**, *29* (4), 1238−1244.

(27) Gao, H. C.; Sun, Y. M.; Zhou, J. J.; Xu, R.; Duan, H. W. Mussel-Inspired Synthesis of Polydopamine-Functionalized Graphene Hydrogel as Reusable Adsorbents for Water Purification. *ACS Appl. Mater. Interfaces* **2013**, *5* (2), 425−432.

(28) Honty, M.; De Craen, M.; Wang, L.; Madejova, J.; Czimerova, A.; Pentrak, M.; Stricek, I.; Van Geet, M. The Effect of High Ph Alkaline Solutions on the Mineral Stability of the Boom Clay - Batch Experiments at 60 Degrees C. *Appl. Geochem.* **2010**, *25* (6), 825−840.

(29) Chiu, C. W.; Lin, J. J. Self-Assembly Behavior of Polymer-Assisted Clays. *Prog. Polym. Sci.* **2012**, *37* (3), 406−444.

(30) Nicolosi, V.; Chhowalla, M.; Kanatzidis, M. G.; Strano, M. S.; Coleman, J. N. Liquid Exfoliation of Layered Materials. *Science* **2013**, *340* (6139), 1226419.

(31) Sureshkumar, M.; Lee, C. K. Polydopamine Coated Magnetic-Chitin (Mct) Particles as a New Matrix for Enzyme Immobilization. *Carbohydr. Polym.* **2011**, *84* (2), 775−780.

(32) Zheng, R.; Wang, S.; Tian, Y.; Jiang, X. G.; Fu, D. L.; Shen, S.; Yang, W. L. Polydopamine-Coated Magnetic Composite Particles with an Enhanced Photothermal Effect. *ACS Appl. Mater. Interfaces* **2015**, *7* (29), 15876−15884.

(33) Bostick, B. C.; Vairavamurthy, M. A.; Karthikeyan, K. G.; Chorover, J. Cesium Adsorption on Clay Minerals: An Exafs Spectroscopic Investigation. *Environ. Sci. Technol.* **2002**, *36* (12), 2670−2676.

(34) Kim, Y.; Kim, Y. K.; Kim, S.; Harbottle, D.; Lee, J. W. Nanostructured Potassium Copper Hexacyanoferrate-Cellulose Hydrogel for Selective and Rapid Cesium Adsorption. *Chem. Eng. J.* **2017**, *313*, 1042−1050.

(35) Fei, B.; Qian, B. T.; Yang, Z. Y.; Wang, R. H.; Liu, W. C.; Mak, C. L.; Xin, J. H. Coating Carbon Nanotubes by Spontaneous Oxidative Polymerization of Dopamine. *Carbon* **2008**, *46* (13), 1795−1797.

(36) Yang, L. P.; Phua, S. L.; Teo, J. K. H.; Toh, C. L.; Lau, S. K.; Ma, J.; Lu, X. H. A Biomimetic Approach to Enhancing Interfacial Interactions: Polydopamine-Coated Clay as Reinforcement for Epoxy Resin. *ACS Appl. Mater. Interfaces* **2011**, *3* (8), 3026−3032.

(37) Yang, H. J.; Sun, L.; Zhai, J. L.; Li, H. Y.; Zhao, Y.; Yu, H. W. In Situ Controllable Synthesis of Magnetic Prussian Blue/Graphene Oxide Nanocomposites for Removal of Radioactive Cesium in Water. *J. Mater. Chem. A* **2014**, *2* (2), 326−332.

(38) Niu, H. Y.; Wang, S. H.; Zeng, T.; Wang, Y. X.; Zhang, X. L.; Meng, Z. F.; Cai, Y. Q. Preparation and Characterization of Layer-by-Layer Assembly of Thiols/Ag Nanoparticles/Polydopamine on Pet Bottles for the Enrichment of Organic Pollutants from Water Samples. *J. Mater. Chem.* **2012**, *22* (31), 15644−15653.

(39) Tawil, N.; Sacher, E.; Boulais, E.; Mandeville, R.; Meunier, M. X-Ray Photoelectron Spectroscopic and Transmission Electron Microscopic Characterizations of Bacteriophage-Nanoparticle Complexes for Pathogen Detection. *J. Phys. Chem. C* **2013**, *117* (40), 20656−20665.

(40) Lin, Y. H.; Fryxell, G. E.; Wu, H.; Engelhard, M. Selective Sorption of Cesium Using Self-Assembled Monolayers on Mesoporous Supports. *Environ. Sci. Technol.* **2001**, *35* (19), 3962−3966.

(41) Chai, L. Y.; Wang, T.; Zhang, L. Y.; Wang, H. Y.; Yang, W. C.; Dai, S.; Meng, Y.; Li, X. R. A Cu-M-Phenylenediamine Complex Induced Route to Fabricate Poly(M-Phenylenediamine)/Reduced Graphene Oxide Hydrogel and Its Adsorption Application. *Carbon* **2015**, *81*, 748−757.

(42) Yu, H. R.; Hu, J. Q.; Liu, Z.; Ju, X. J.; Xie, R.; Wang, W.; Chu, L. Y. Ion-Recognizable Hydrogels for Efficient Removal of Cesium Ions from Aqueous Environment. *J. Hazard. Mater.* **2017**, *323*, 632−640.

(43) Hassan, M.; Wu, D. D.; Song, X. D.; Ren, S. Z.; Hao, C. Synergistic Effect of Heat Treatment and Concentration of Polydopamine Enhance the Electrochemical Performances of Hollow Nitrogen-Doped Carbon Microspheres. *Ionics* **2019**, *25* (10), 4685−4701.

(44) Lee, W.; Lee, J. U.; Jung, B. M.; Byun, J. H.; Yi, J. W.; Lee, S. B.; Kim, B. S. Simultaneous Enhancement of Mechanical, Electrical and Thermal Properties of Graphene Oxide Paper by Embedding Dopamine. *Carbon* **2013**, *65*, 296−304.

(45) Chen, S. Q.; Hu, J. Y.; Shi, J.; Wang, M. X.; Guo, Y. F.; Li, M. L.; Duo, J.; Deng, T. L. Composite Hydrogel Particles Encapsulated Ammonium Molybdophosphate for Efficiently Cesium Selective Removal and Enrichment from Wastewater. *J. Hazard. Mater.* **2019**, *371*, 694−704.

(46) Dwivedi, C.; Pathak, S. K.; Kumar, M.; Tripathi, S. C.; Bajaj, P. N. Preparation and Characterization of Potassium Nickel Hexacyanoferrate-Loaded Hydrogel Beads for the Removal of Cesium Ions. *Environ. Sci-Wat Res.* **2015**, *1* (2), 153−160.

(47) Lee, I.; Park, C. W.; Yoon, S. S.; Yang, H. M. Facile Synthesis of Copper Ferrocyanide-Embedded Magnetic Hydrogel Beads for the Enhanced Removal of Cesium from Water. *Chemosphere* **2019**, *224*, 776−785.

(48) Isobe, N.; Chen, X. X.; Kim, U. J.; Kimura, S.; Wada, M.; Saito, T.; Isogai, A. Tempo-Oxidized Cellulose Hydrogel as a High-Capacity and Reusable Heavy Metal Ion Adsorbent. *J. Hazard. Mater.* **2013**, *260*, 195−201.

(49) Deepthi Rani, R.; Sasidhar, P. Sorption of Cesium on Clay Colloids: Kinetic and Thermodynamic Studies. *Aquat. Geochem.* **2012**, *18* (4), 281−296.

(50) Kang, K. C.; Linga, P.; Park, K. N.; Choi, S. J.; Lee, J. D. Seawater Desalination by Gas Hydrate Process and Removal Characteristics of Dissolved Ions (Na+, K+, Mg2+, Ca2+, B3+, Cl-, So42-). *Desalination* **2014**, *353*, 84−90.

(51) Jang, J.; Lee, D. S. Enhanced Adsorption of Cesium on Pva-Alginate Encapsulated Prussian Blue-Graphene Oxide Hydrogel Beads in a Fixed-Bed Column System. *Bioresour. Technol.* **2016**, *218*, 294−300.

(52) Naeimi, S.; Faghihian, H. Performance of Novel Adsorbent Prepared by Magnetic Metal-Organic Framework (Mof) Modified by Potassium Nickel Hexacyanoferrate for Removal of Cs+ from Aqueous Solution. *Sep. Purif. Technol.* **2017**, *175*, 255−265.

(53) Zhang, H.; Hodges, C. S.; Mishra, P. K.; Young, J. Y.; Hunter, T. N.; Lee, J. W.; Harbottle, D. Bio-Inspired Preparation of Clay−Hexacyanoferrate Composite Hydrogels as Super Adsorbents for $Cs^{+}$: dataset University of Leeds. [Dataset]. 2020, https://doi.org/10.5518/838.